

JGR Space Physics

RESEARCH ARTICLE

10.1029/2021JA029787

Key Points:

- Separation of temporal/spatial variations in sporadic sodium layer (SSLs) is observed by a three-directional lidar system at Zhongshan, Antarctica
- The formation and perturbation of SSLs are associated with a sporadic E layer at the same height
- The SSLs are advected by the background wind

Correspondence to:



X. Chen and W. Huang,
chenxiangcai@pric.org.cn;
huangwentao@pric.org.cn

Citation:

Chen, X., Huang, W., Ban, C., Kosch, M. J., Murphy, D. J., Hu, Z., et al. (2021). Dynamic properties of a sporadic sodium layer revealed by observations over Zhongshan, Antarctica: A case study. *Journal of Geophysical Research: Space Physics*, 126, e2021JA029787. <https://doi.org/10.1029/2021JA029787>

Received 13 JUL 2021
 Accepted 26 OCT 2021

Dynamic Properties of a Sporadic Sodium Layer Revealed by Observations Over Zhongshan, Antarctica: A Case Study

Xiangcai Chen¹ , Wentao Huang¹ , Chao Ban², Michael J. Kosch^{3,4,5} , Damian J. Murphy⁶, Zejun Hu¹ , Jianjun Liu¹ , Fang He¹, Rui Wang¹ , Huigen Yang¹ , and Hongqiao Hu¹

¹MNR Key Laboratory for Polar Science, Polar Research Institute of China, Shanghai, China, ²Key Laboratory of Middle Atmosphere and Global Environment Observation, Institute of Atmospheric Physics, Chinese Academy of Science, Beijing, China, ³Department of Physics, Lancaster University, Lancaster, UK, ⁴South African National Space Agency, Hermanus, South Africa, ⁵Department of Physics and Astronomy, University of the Western Cape, Cape Town, South Africa, ⁶Department of Agriculture, Water and the Environment, Antarctic Climate Program, Australian Antarctic Division, Kingston, TAS, Australia

Abstract A sodium Doppler lidar system with three-directional measurements of sodium density, atmospheric wind field, and temperature was established at Zhongshan (69.4°S, 76.4°E), Antarctica. On November 14, 2019, a sporadic sodium layer (SSL) was observed at an altitude range of 93–103 km. The temporal/spatial sodium density variations of this SSL are associated with a strong sporadic E (E_s) layer at nearly the same height, which is modulated by the convective electric field. By considering the structures and the time lags of the SSL's growth at three positions, the SSL appears to have a horizontal advection in an approximately westward direction with a velocity of the order of 80 m/s. This is consistent with the zonal wind velocity derived from the lidar system itself. The temporal/spatial sodium density variations strongly indicate that the formation and perturbation of SSLs are related to the evolution of E_s layers due to varied electric fields and atmospheric gravity waves, while it is advected by the horizontal wind.

Plain Language Summary A sporadic E layer (E_s) could be formed by metallic ions and then modified or transported by the action of magnetospheric electric fields in the high latitude ionosphere. It has been widely proposed that E_s layers play an important role in the formation of sporadic sodium layers (SSL), but detailed studies of their dynamic process and evolution are still lacking. A three-frequency Sodium (Na) resonance fluorescence Doppler lidar has been recently deployed by the Polar Research Institute of China, which could measure the sodium density, temperature, and wind profiles simultaneously in three directions. To clarify the dynamic properties of E_s /SSL, we have performed observations of an event at Zhongshan Station (69.4°S, 76.4°E), Antarctica, which includes sodium density profiles and wind velocity measured by the multidirectional lidar system, detection of the E_s layer by a collocated Digisonde radar, F region ion velocity, that is, electric field, derived by the SuperDARN HF radar network, as well as gravity wave perturbations determined from the Davis medium frequency radar.

1. Introduction

Since the discovery of a sporadic sodium layer (SSL) that was superposed on a normal sodium layer in the mesosphere/lower thermosphere (MLT; Clemesha et al., 1978), numerous SSL events have been reported (cf. Clemesha, 1995; Qiu et al., 2016; and references therein). The SSLs, with rapid growth of the sodium atom density over a narrow height range (e.g., Clemesha, 1995; Tsuda et al., 2011), usually show an extended life span from a few tens of minutes to several hours (e.g., Batista et al., 1991; Cox & Plane, 1998). One of the interests in SSL studies is thus exploring the generation mechanism for SSLs and understanding the controlling factors of their temporal and spatial evolution.

Ionospheric sporadic E (E_s) layers have been widely accepted as a good candidate for the source of sodium atoms in SSLs (e.g., Cox & Plane, 1998; Kirkwood & Zahn, 1991; Takahashi et al., 2015). Some good correlations between the occurrence of SSLs and E_s layers have also been reported (cf. Croskey et al., 2006; Dou et al., 2009, 2010; Heinselman et al., 1998). Rocket-borne mass spectrometric measurements have

demonstrated that the E_s layers consist of metallic ions (Grebowsky & Aikin, 2002; Kopp, 1997), such as Fe^+ , Mg^+ , Na^+ , etc., and can be vertically driven by the neutral wind and/or the electric field (Kirkwood & Zahn, 1991). When horizontal and vertical convergence of ions occurred under some conditions (e.g., MacDougall & Jayachandran, 2005), the E_s layers could descend/ascend in altitude, such as due to the atmospheric tide and/or gravity waves (e.g., MacDougall et al., 2000). As the atmospheric density increases exponentially with decreasing altitude, the rate of ion neutralization increases rapidly at lower heights (Collins et al., 2002); hence a neutral SSL could thus form via this rapid ion neutralization (Cox & Plane, 1998).

The other candidates for the source of sodium atoms could be direct meteor deposition, and/or release from aerosol particles, as well as redistribution of existing atoms (e.g., Batista et al., 1991; Clemesha, 1995; Clemesha et al., 1978). However, direct meteor deposition requires a meteor shower with a large mass, and aerosol particle release requires a background temperature increase (Qiu et al., 2015, 2018). The redistribution of existing atoms is another good explanation for SSLs. Using a steerable sodium lidar system at Winkfield (51.4°N, 0.7°W) that pointed sequentially in three different directions (at zenith angles of 30°). Thomas et al. (1977) first observed clear evidence of a horizontal variation of the sodium concentration near the peak of the normal layer. Based on steerable lidar system observations at São José dos Campos (23°S, 45°W), Batista et al. (1991) systematically investigated sodium density variations in 12 SSL events at three horizontal positions. There was no case where the advent of SSLs occurred simultaneously at all three positions; time lags of each SSL among the different positions were always observed. The inferred horizontal velocities from the time lags of SSLs were mostly less than 100 m/s, except for one case observed by Clemesha et al. (1980) with a velocity of the order of 200 m/s. However, their hypothesis of horizontal advection was not confirmed by background wind observations.

In a recent study, an SSL event detected with a five-directional lidar system was reported by Tsuda et al. (2015). By utilizing the SSL onset time differences recorded at the five positions, the horizontal velocity of the SSL was derived and compared with the background wind velocity from the collocated meteor radar and European Incoherent Scatter radar (Tsuda et al., 2015). They found both velocities were consistent. Moreover, the amount of the sodium atom increase at the five positions was mostly equal, which strongly indicates that the observed SSL was just advected by the background wind. Nevertheless, the end time of the SSL event was not observed by Tsuda et al. (2015) due to the sky becoming cloudy.

Although a causal link between the E_s layer and SSL has been observed and reported (e.g., Heinselman et al., 1998; Kirkwood & Collis, 1989; Kirkwood & Zahn, 1991), how the temporal and spatial variations of SSL relate to the evolution of the E_s layers and the horizontal advection by background wind is still unclear. Comprehensive evaluation of the sodium atom production process in a SSL and its related temporal and spatial variations with the E_s layer and background wind is still an important open question.

Since February 2019, a three-frequency sodium resonance fluorescence Doppler lidar system has been operating at Zhongshan Station (ZHS, 69.4°S, 76.4°E), Antarctica. With three-directional beams pointing toward the zenith, and 30° off-zenith to the south and west, this system can obtain sodium density, line-of-sight wind, and temperature at three positions simultaneously. In this article, an SSL event on November 14, 2019 that was detected by this lidar system is analyzed. We have performed detailed observations to clarify the temporal and spatial variations of the SSL, including the E_s layer detected by a collocated DPS-Digisonde, electric field measurements by the Super Dual Auroral Radar Network (SuperDARN; e.g., Ruohoniemi & Baker, 1998), as well as wind velocity by the lidar system itself. In addition, the 1.94 MHz medium frequency (MF) radar (e.g., Reid et al., 2018) data from Davis station (68.6°S, 78.0°E), which lies ~116 km northeast of ZHS, is used to assess the gravity wave activity below the SSL when it occurs. All these observations are combined to better understand the rapid sodium atom production process and its related dynamic properties in the MLT region. In Section 2, we will briefly describe instruments and data sets. The observational results are presented in Section 3, while possible generation processes and mechanisms of SSLs are discussed and proposed in Section 4. This article finally ends with a summary in Section 5.

2. Instruments and Data Sets

2.1. The Sodium Lidar

The three-frequency Sodium (Na) resonance fluorescence Doppler lidar at ZHS mainly consists of the lidar transmitter, receiver, data acquisition and system control modules. The lidar laser pulses are produced by a four-stage pulsed dye amplifier seeded with a state-of-the-art 589 nm frequency-doubled solid-state diode laser. As required by the classic three-frequency probing technique (Chu & Papen, 2005 and reference therein), the seed laser is locked to one of the Na D_{2a} Doppler-free saturation absorption features within ± 2 MHz, and then sequentially shifted ± 630 MHz by a free-space acoustic-optical modulator. Three 82-cm diameter microcrystal-glass substrate telescopes with parabolic reflecting surface are used to receive returning lidar photons in three directions, that is, the zenith, 30° off-zenith to the south, and 30° off-zenith to the west, for wind field measurements, respectively. An ultra-narrow Na Faraday filter is implemented to suppress the solar background during daytime for continuous diurnal operation. With transmitted laser power of about 0.55 W in each direction, lidar signal photons collected by the receiving telescopes were detected by photomultiplier tubes, integrated and recorded for 15 s with a 45 m range resolution. The uncertainties in temperature and vector wind measurements induced by photon noise, around the peak of Na layer (at ~ 90 km) with 1 hr and 0.5 km resolutions, can achieve less than ± 0.3 K and ± 1.6 m/s for nighttime and ± 1.0 K and ± 2.8 m/s for daytime observations, respectively.

2.2. The Ionosonde Radar (DPS-4D)

The Digisonde Portable Sounder (DPS-4D) operated at ZHS can be used to monitor the overhead ionosphere. It uses one simple crossed delta antenna for transmission, and four crossed magnetic dipole antennas for reception. Using six digitally synthesized off-vertical reception beams in addition to the vertical beam, the DPS-4 Digisonde can operate in multibeam sounding mode (Reinisch et al., 2009). For each frequency-range pixel, the beam with the maximum amplitude is selected, and the amplitude and beam numbers are recorded in the output data (Reinisch et al., 2008). Currently, the Digisonde operates at 0.05 MHz frequency step from 0.5 to 9.5 MHz and a range resolution of 2.5 km from 80 to 640 km (virtual height), while the ionograms are recorded at a time interval of 7.5 min. By manually scaling the ionograms via the SAO software, ionospheric characteristics parameters, such as E_s critical frequency (f_oE_s) and virtual height ($h'E_s$) can be obtained.

2.3. The SuperDARN Radar

The combined fields of view of the SuperDARN radar network cover the majority of the northern and southern hemisphere polar regions. Utilizing HF radio wave refraction to achieve orthogonality with the Earth's magnetic field in the E - and F -region ionosphere, field-aligned irregularities at ~ 10 m Bragg scale produce maximum backscatter power (Milan et al., 1997). From the received signal-to-noise ratios the ionospheric plasma Doppler line-of-sight velocity, the Doppler spectral power, and the Doppler spectral width can be derived (Greenwald et al., 1995). Based on all the available line-of-sight velocity data and merging it from pairs of radars within common-volume areas (Ruohoniemi & Baker, 1998), a large-scale plasma convection map is produced covering the high-latitude ionosphere. From this, the global convection electric field can also be obtained (see Chisham et al., 2007 for more details).

2.4. The MF Radar at Davis

The MF radar at Davis station (68.6°S , 62.9°E) lies ~ 116 km northeast of ZHS and can be used to measure the strength of turbulence through velocity variances (Murphy & Vincent, 2000). The MF radar consists of a square transmitting array ($\sim 40^\circ$ in beam half-width at half maximum) and three cross-dipole receiving arrays. By operating in space-antenna mode at a frequency of 1.94 MHz and using pulsed transmission with half-power full pulse widths of 30 μs , the three complex time series were analyzed using full correlation analysis to produce wind measurements. The horizontal wind components are theoretically sampled at 2 km intervals between the heights of 64 and 102 km.

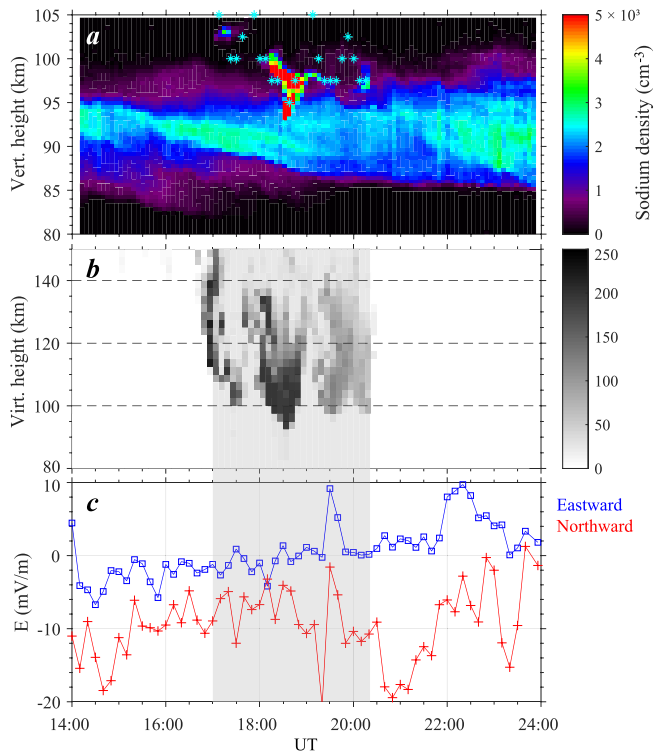


Figure 1. (a) Height-time intensity variations of the sodium density from 14:00 to 24:00 UT on November 14, 2019 between 80 and 105 km. Blue asterisks denote the height of the E_s layer derived from the DPS-4 Digisonde. (b) The number of ionospheric echoes recorded by the colocated DPS-4 Digisonde in the E layer at frequencies from 3 to 9.5 MHz. (c) The corresponding electric field derived from SuperDARN data. The blue and red lines represent eastward and northward components, respectively. In this study, we mainly focus on the sporadic sodium layer (SSL) occurring for time intervals shown in the gray shade (i.e., 17:00–20:20 UT).

3. Observation Results

A 10-hr continuous daytime observation by lidar and radar was made on November 14, 2019 from 14:00 to 24:00 UT (UT = MLT [Magnetic Local Time] – 1.75 hr; UT = LT – 5 hr). The temporal and altitude variation of the sodium density profile from the vertical beam, with a 5 min time and a 450 m altitude resolution, is shown in Figure 1a. The number of simultaneous ionospheric echoes recorded by the colocated DPS-4 Digisonde in the E layer at 130 frequencies from 3 to 9.5 MHz, with 7.5 min time and 2.5 km height resolution, is shown in Figure 1b as a function of virtual height and UT time. By manually scaling the E_s layer, the height variations of the layer are overlaid in Figure 1a (i.e., blue asterisks). Figure 1c shows the corresponding electric field with 10 min time resolution in the northward and eastward components over ZHS derived from the SuperDARN data.

From Figure 1a, it can be seen that the normal sodium layer occurs at altitudes of ~85–95 km. Starting at 17:00 UT, there is an isolated enhanced sodium density layer (i.e., the so-called SSL) observed at around 101 km, which gradually ascends to about 103 km by 17:30 UT. Half an hour later, a particular region with much higher sodium density at 93–100 km until 19:15 UT can be easily identified. These regions with maximum sodium density of $\sim 3.2 \times 10^{10} \text{ m}^{-3}$ are about 10 times higher than the normal sodium layer density. We notice that this SSL exists in two separated layers with different altitudes. One above 96 km with a descending trend, and the other below it with an ascending trend. After 20:00 UT, an SSL with a short time duration of about 10 min is observed at an altitude of 97 km.

The sodium density of the SSL observed from 17:00 to 20:20 UT changed significantly with time and altitude. This is almost consistent with the occurrence and variations of ionospheric echoes for the E_s layer. The strongest SSL observed during the time interval of 18:10–19:00 UT corresponds to a large number of ionospheric echoes at almost the same height. The number of ionospheric echoes decreases at higher altitudes around 17:45 and 19:05 UT, which time interval precisely corresponds to the decreased sodium density at the upper levels. Moreover, the starting and ending

times of the SSLs observed from the lidar vertical beam (indicated by the gray shading in Figure 1) are aligned to the appearance and disappearance of the E_s layer. This implies that the E_s layer provides the source of sodium atoms to the SSL. From plasma convection observations by SuperDARN over Antarctica during the SSL/ E_s time interval, the strength of the horizontal electric field over ZHS is less than $\sim 12 \text{ mV/m}$ (see Figure 1c), except for time at 19:20 UT, and is dominated by an eastward horizontal ion flow in the F region with velocities less than 170 m/s (i.e., $\mathbf{E} = \mathbf{v} \times \mathbf{B}$, assuming the geomagnetic field $5.4 \times 10^5 \text{ nT}$). This means that the SSL/ E_s is located in the duskside convection cell.

To investigate the relationship between the SSLs sodium density and ionospheric E_s layer variations in more detail, Figure 2a shows variations of the SSL's maximum sodium density from 16:30 to 20:30 UT between 93 and 103 km. Figure 2b represents the ratio of the maximum sodium density to the background normal sodium density in the same altitude range. The background normal sodium density is the averaged value between 14:30 and 16:30 UT at each altitude where the sodium density varied smoothly with time. We should notice that both sodium density in Figure 2a and the ratio in Figure 2b are plotted with an exponential scale on the Y-axis. The critical frequency of the E_s layer (f_oE_s) is shown in Figure 2c. The altitude of the maximum sodium density is shown in Figure 2d (blue line), while the E_s layer-related virtual height variations (i.e., $h'E_s$), with a 2.5 km error bar indicating possible manual scaling errors, are also overlaid.

The SSL starts at an altitude of around 102.5 km, and the maximum sodium density increases from $\sim 1.0 \times 10^9$ to $\sim 3.4 \times 10^9 \text{ m}^{-3}$ within 10 min between 17:02 and 17:12 UT. Soon thereafter, the maximum sodium

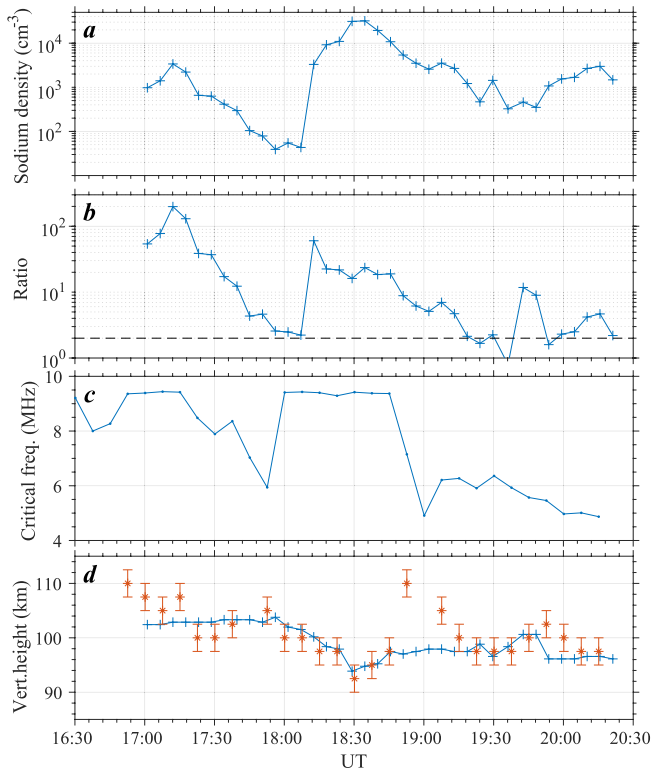


Figure 2. (a) Variations of the sporadic sodium layer (SSL)'s maximum sodium density from 16:30 to 20:30 UT. (b) The ratio of the maximum sodium density to background sodium density at the same altitude. The horizontal black dash line denotes values with a ratio greater than 2. (c) The variations of critical frequency in the E_s layer from the colocated DPS-4 Digisonde. (d) Variations in altitude of the maximum density of the SSL (blue line) and the E_s layer (red asterisks with error bar).

density gradually decreases to $\sim 0.04 \times 10^9 \text{ m}^{-3}$ at an altitude of about 101.5 km until 18:07 UT, which is about twice the background sodium density. A strong SSL with double-layers occurred around 18:30 UT and its maximum sodium density varies from $\sim 3.3 \times 10^9$ to $\sim 3.2 \times 10^{10} \text{ m}^{-3}$, which is about 20 times higher than the background intensity. Finally, before the end of the SSL at 20:15 UT, we find the maximum sodium density is almost equal to the onset of SSLs at 17:05 UT and 18:10 UT, but at a lower height of 96.5 km. From Figure 2c, we observe the ending of the SSL at $\sim 19:00$ UT is associated with the E_s layer weakening with f_oE_s at ~ 5 MHz. This would correspond to an ionospheric electron density of $3.1 \times 10^{11} \text{ m}^{-3}$. Moreover, it can be seen that the enhancement of the E_s layer at 16:55 and 18:00 UT occurs before the onset of the SSL by at least 5 min. Since the Digisonde observation mode was operated over a limited frequency range (i.e., 0.5–9.5 MHz), the ionospheric electron density corresponding to the maximum sodium density of the SSL cannot be properly estimated over this time interval. In Figure 2d, we observe the variations of the SSL height (blue line) are closely associated with the average height of the E_s layer. The correlation coefficients for the SSL height within 5 km (29 points) and 2.5 km (18 points) of the E_s layer are 0.72 and 0.94, respectively. All these observational results strongly indicate that the E_s layer is most likely the source supply of sodium for the SSL in this event. However, it is difficult to explain the formation of SSL with a double layer (i.e., with upper-layer and lower-layer) at 18:30–18:45 UT.

To better understand the dynamic properties of the SSL, Figures 3a–3c show height and time variations of the raw photon count, with temporal and spatial resolutions of 15 s and 45 m, respectively, from the (a) south, (b) vertical, and (c) west beams at 90–100 km during 18:00–19:00 UT. We have normalized the count data with the Rayleigh scattering intensity at the lower height, removing the effects of the fluctuations in the laser power and the transmittance in the lower atmosphere. The normalized raw photon count intensity would thus be in proportion to the sodium number density and the resonance scattering cross-section. The SSLs with upper layer and lower layer located above and below 96 km, respectively,

are observed at all three positions. Both the upper-layer and lower-layer of the SSLs are characterized by an increased photon count with a narrow altitude range (i.e., typically ~ 1 km full width at half maximum). The corresponding time variations in the raw count intensity data for 92–96 km height are also shown in Figures 3d–3f. The red, blue, and black lines represent the mean, median, and peak values of the raw count intensity. (Note that the peak values have been reduced by a factor of 3.) The timings (i.e., onset and ending times) of the SSL lower-layer determined at each beam for both the mean and the medium are denoted by vertical dashed lines in each panel. These times occur when the ratio of the maximum density to the background normal density is greater than 2 (cf. Simonich et al., 2005). For the mean values, it can be seen that the SSL lower-layer first occurred in the south beam at 18:25:42 UT. After 50 s, the enhanced raw photon count is observed by the vertical beam, whereas the onset time in the west beam lagged by 11 min. A similar situation with a time lag of ~ 9.08 min is also observed when comparing the ending time from vertical to west positions. Moreover, by comparing the median values between the vertical and west beams, time lags of ~ 11.82 and ~ 10.73 min for onset and ending time, respectively, are also observed. However, the ending of the SSL lower-layer at the south beam is different. This is due to the ending of the SSL lower layer being accompanied by a wavelike perturbation (see Figure 3a). Considering the time lags for onset and end of the SSL in the raw count intensity variations between the vertical and west beams, it is suggested that the horizontal advection of enhanced sodium density plays an important role for the SSL.

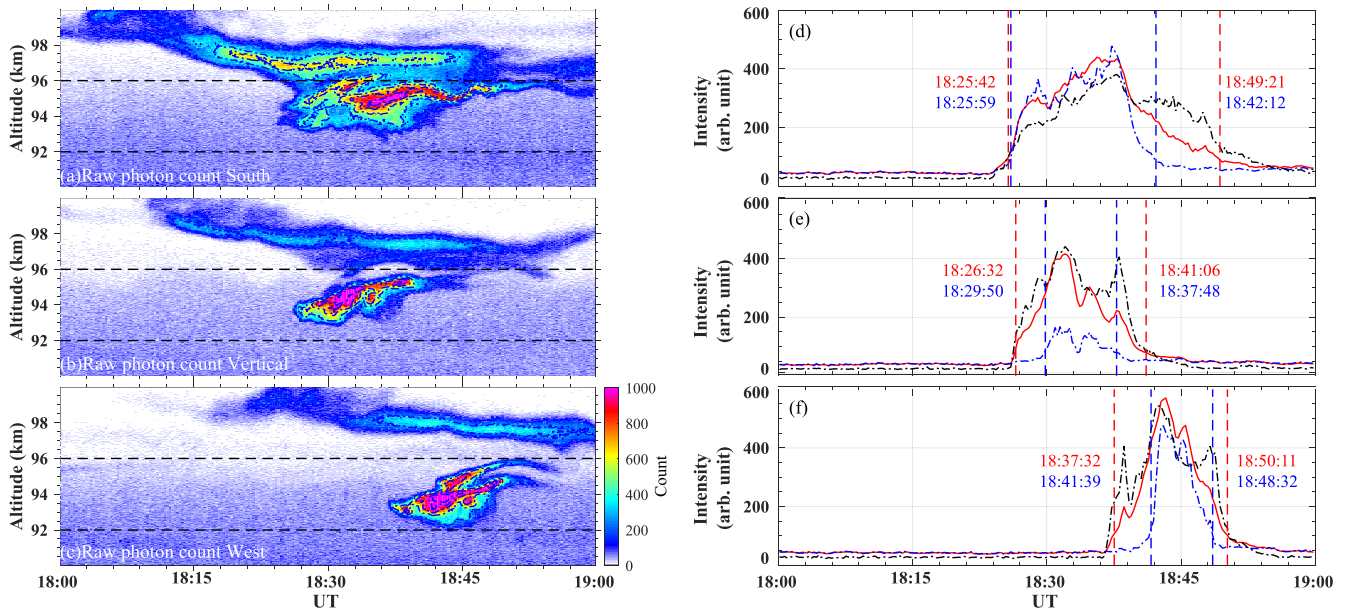


Figure 3. (a–c) Height and time variations of raw photon counts, with 15 s time and 45 m height resolution, from the (a) south, (b) vertical, and (c) west beams. (d–f) The corresponding time variations in the raw count intensity data for 92–96 km height. Red, blue, and black lines represent data obtained with the mean, median, and peak values, respectively. (Note that the peak values have been reduced by a factor of 3). The onset and end times, defined as the time when the intensity became twice that before the event, are shown by vertical dash lines.

4. Discussion

4.1. SSL Production From the E_s Layer

It is important to understand the origin of the source that is producing/providing a large number of sodium atoms for SSLs within a short timescale and a narrow vertical range. In this article, we report an SSL with spatial and temporal variations over Zhongshan, Antarctica. The dynamic process of the SSL is closely associated with the evolution of the E_s layer, which means that the conversion of sodium ions to sodium atoms in the E_s layer occurred. Previous studies have discussed the E_s layer as a major source for high-density SSLs appearing between 90 and 100 km. Kane et al. (1993) estimated that the sodium ion abundance in an E_s layer was 10% of that of the atoms at most, while a 4% assumption for the sodium ion abundance was an underestimation (Hansen & von Zahn, 1990). In our observations, the SSL occurring after 18:10 UT is at a height below 100 km and the SSL and E_s layer have a good height correlation. An SSL-related sodium density more than twice higher than the background intensity is observed at 18:10–18:45 UT and 20:10–20:15 UT (see Figure 2b). The averaged maximum sodium density of the SSLs (using an altitude resolution of 0.45 km) at these time intervals are $\sim 1.67 \times 10^{10}$ and $\sim 2.8 \times 10^9 \text{ m}^{-3}$, respectively. If we assume that the averaged maximum sodium density is charge exchanged from sodium ions in the E_s layer at the 10% rate noted above, this should correspond to an ionospheric density of at least $\sim 1.67 \times 10^{11}$ and $\sim 2.8 \times 10^{10} \text{ m}^{-3}$ at the same height. During these intervals, the E_s layer with f_0E_s more than 5 MHz (i.e., $\sim 3.1 \times 10^{11} \text{ m}^{-3}$) is always observed. This means that the hypothesis that the E_s layer alone can provide enough of a supply of sodium atoms in this event is plausible.

Simultaneous ground-based sodium lidar and ionosonde observations of SSL and E_s layers in time and spatial location have been extensively studied by previous authors (e.g., Dou et al., 2009; von Zahn & Hansen, 1988; Williams et al., 2007). Although the E_s layer is expected to be acting as the sodium reservoir, and a strong correlation of simultaneous occurrence of SSLs and E_s layers was observed, the sodium ion chemistry seemed to not provide a satisfactory explanation for the fast rise of sodium atom density within the growth phase of SSLs with time constants of 5 min (von Zahn & Hansen, 1988). For our current study, the growth phase of the SSLs had typical time constants of 10–15 min (see Figure 2a, i.e., the time duration from onset to the maximum of the SSL), and the electron density enhancement of the E_s layer always preceded the sodium enhancement (see Figures 2a and 2c), which means that our E_s layer is the source

Table 1
Estimates of Average Descent Velocity of the E_s Layers

Time interval (hh:mm:ss)	Initial height (km)	Ending height (km)	Descending velocity (m/s)
16:45:10–17:30:10	120	100	~7.41
17:37:40–18:30:10	122.5	92.5	~9.52
19:00:10–19:30:10	122.5	97.5	~13.89
19:52:40–20:15:10	102.5	97.5	~3.7

of sodium for the SSL. From a statistical point of view, the seasonal dependence of SSL occurrence correlates well with the annual variation of E_s , as studied by Dou et al. (2010). A “meteor-Es-SSL” chain responsible for the recombination process was taken into consideration by them. However, because meteoric ablation should simultaneously generate sodium and electron density enhancements at the same altitude (Clemesha et al., 1978), the observed pre-existing E_s layer with wavelike fluctuations should rule out direct meteor deposition as the cause of the SSL.

To exclude the possible redistribution of the background layer resulting in SSLs, the time-sequential relationship of the SSL/ E_s is investigated in more detail. Table 1 gives the estimates of the average descent velocity

of the E_s layer for the four-time intervals at the lower E region. Comparing these times to the SSL onset times of ~17:02, ~18:30, and ~20:00 UT at the altitudes of ~101, ~93, and ~97 km, it seems likely that the descent of the E_s layer would trigger the release of sodium atoms, while its height variations regulate the SSL's lifetime. A theoretical explanation proposed by Cox and Plane (1998) has shown that sodium ions can be neutralized via an ion-molecule mechanism which describes the conversion of sodium ions to atomic sodium in a descending E_s layer. Similar observational events were also reported by previous studies (Beatty et al., 1989; Kane et al., 1993; Williams et al., 2007). By identifying the vertical and temporal structures of the SSL sodium and the E_s layer electron density, Kane et al. (1993) found the electron enhancement and the sodium enhancement at an altitude of 93–97 km were in phase. In our event, sodium enhancements always correlate with the descent of the E_s layer. The high correlation between the altitude and abundance variations of the SSL and E_s layers illustrates that the SSL formation is strongly related to descending E_s layer and most likely involves the neutralization of sodium ions.

4.2. SSL/ E_s Related Dynamics and Electrodynamics

Dynamic processes are evident in the temporal and spatial wavelike structures of the SSL/ E_s layers. With the thin E_s layer declining into the E region, both the electric field and neutral wind are expected to modulate the E_s layer (e.g., Nygrén et al., 1984, 2008). According to dynamic and electrodynamic theory (Kirkwood & Nilsson, 2000), the vertical motion of the ion is governed by electric fields, neutral wind, gravity, and ambipolar diffusion. Ignoring ion diffusion due to gradients in the plasma pressure and to the force of gravity, the vertical motion of ions can be expressed as:

$$v_{iz} = \frac{1}{1+r_i^2} \left[\frac{E_E}{B_0} + W_N \sin I \right] \cos I + \frac{r_i}{1+r_i^2} \left[-\frac{E_N}{B_0} + W_E \right] \cos I + \left[1 - \frac{\cos^2 I}{1+r_i^2} \right] W_Z \quad (1)$$

where v_{iz} is the vertical motion of ion (positive downward), r_i is the ratio of the ion-neutral collision frequency to the ion gyrofrequency, E_E and E_N represent the eastward and northward components of the electric field, and W_N , W_E , and W_Z are the horizontal (northward and eastward) and vertical (positive downward) components of the neutral wind. The magnetic dip angle I is 71.6° at ZHS. The ion motion above 120–130 km is dominated by the first term (i.e., eastward electric field and meridional wind) because the ion gyro-frequency exceeds the collision frequency, while the zonal wind and north-south component of the electric field control ion motion at heights below 100–110 km through the second term. Moreover, when an atmospheric gravity wave exists, the third term may be significant at any height in the presence of strong vertical motion. The present SSL/ E_s event mainly occurs in altitude range of 93–100 km with a southward electric field, and both the zonal wind and gravity waves contribute to the vertical motion of the E_s layer.

The contours of the zonal and meridional wind observed by the lidar system between 14:00 and 24:00 UT are illustrated in Figures 4a and 4b, respectively. Wind variations with height are shown in Figure 4c for 17:30 to 19:30 UT. The zonal wind shows a persistent westward velocity at the heights of 92.5–97 km until 20:00 UT, while a downward propagating phase structure is apparent in the wind. Kirkwood and Nilsson (2000) studied the relative contributions of the electric field and neutral wind for the second term in Equation 1. A strong wind of 100 m/s has almost the same effect as a rather small electric field of only 5 mV/m. During the time interval of 17:00–20:15 UT the northward electric field had a median value of -8.7

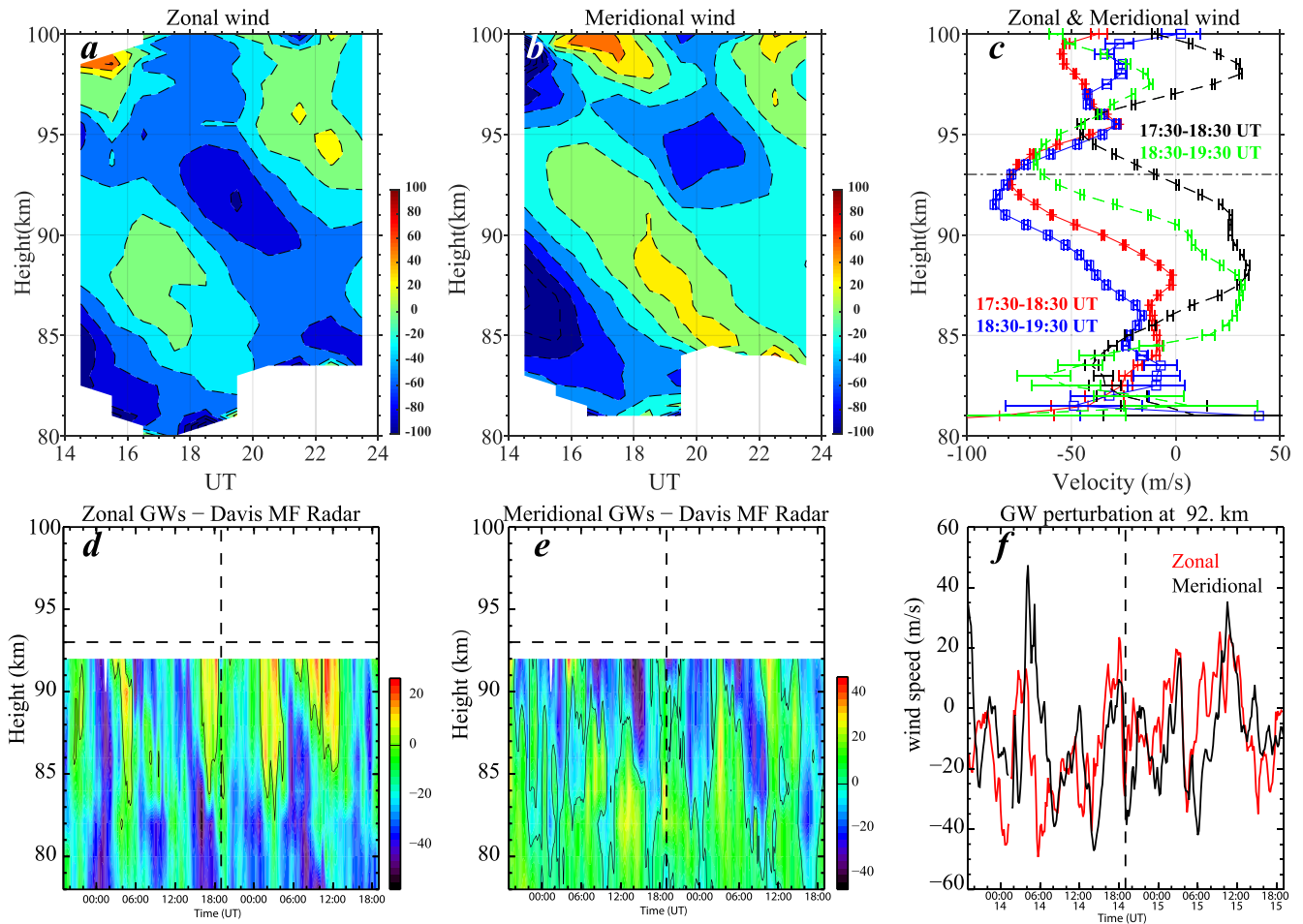


Figure 4. Time-height contours of the zonal (a) and meridional (b) winds between 14:00 and 24:00 UT derived from the sodium lidar. The data have been smoothed to have a vertical resolution of 0.5 km and a temporal resolution of 1 hr for the wind field. (c) Profiles of zonal (red and blue) and meridional (black and green) winds at 17:30–18:30 and 18:30–19:30 UT. Zonal (d) and meridional (e) 10 min average winds from the Davis MF radar for 2 days around the Zhongshan Station (ZHS) sporadic sodium layer (SSL) occurrence. The tidal variations have been removed with the gravity wave activity remaining. (f) Zonal (red) and meridional (black) perturbation winds at 92 km.

(± 4.1) mV, assuming a zonal wind with a constant velocity of -50 m/s and adopting the height-dependent ratio r_i (Xue et al., 2013, see their Figure 5a), the combined electric field and neutral wind will result in the E_s layer descending with a speed of ~ 7.82 (± 6.04) m/s at 110 km and ~ 0.42 (± 0.32) m/s at 95 km. This is consistent with the estimates of the average descent velocity of the E_s layers shown in Table 1, which implies that the vertical wind velocity decreased sharply with decreasing altitude. An accumulation of metal ions and/or electrons modulated by the varied north-south electric field component and zonal wind at a certain altitude would be expected.

The downward propagating phase structure of horizontal wind implies that the formation of the SSL/ E_s layers could also be related to atmospheric gravity wave activity. MacDougall et al. (2000) suggested that such atmospheric wave motion is very efficient in moving ionization up or down, particularly at lower heights. The ionization will be concentrated near the gravity wave nulls, with a downward motion from above and upward motion from below. This process has been observed in this event at around 18:30 UT at a height of ~ 93 km, where the sodium density is largest. During this interval, the SSL upper layer is descending with the downward motion of the E_s layer, followed by the SSL lower layer ascending.

To assess the gravity wave activity, the 1.94 MHz MF data from Davis station, which lies ~ 116 km northeast of ZHS, has been analyzed. To balance short-term variations against the quality of tidal fit, a 4-day window of hourly averaged winds is chosen to calculate the amplitude and time of the maximum of the diurnal,

semidiurnal, and terdiurnal components of the zonal and meridional winds. These fitted parameters are then used to reconstruct the underlying tidal wind field over a 2-day interval centered on the occurrence of the SSL. The MF radar wind determinations were averaged into 10 min bins over the days surrounding the ZHS SSL event. Tidal fits were made to a 4-day interval of these data and the reconstructed tides were removed from the time series (Murphy, 2002). The resulting perturbation winds, with a three-point smoothing applied, are thus shown in Figure 4d (zonal) and Figure 4e (meridional), while the corresponding perturbation velocities at 92 km are shown in Figure 4f. Downward propagating phase structures are apparent in the upper levels of Figures 4d and 4e suggesting the presence of an upward propagating gravity wave. These phase structures are steep, with rapid velocity transitioning from positive to negative at the time of the SSL, indicating a large vertical wavelength node at the observed heights. The gravity wave activity illustrated by the MF radar data at the nearby station suggests such atmospheric wave motions could also modulate the temporal and spatial variations of the SSL intensities.

In comparison to 5 min averaged data shown in Figure 1a, there is another interesting feature that the 15 s data in Figure 3 reveals considerably more fine structures of the SSL. In Figures 3a–3c, the double layers of the SSL show predominant wavelike structures with periods of 7–11 min at 96–100 km and ~3–4 min at 94–96 km, which is especially evident in the south direction in Figure 3a. This is very different from the observations of the E_s layer by the ionosonde and the gravity wave by the MF radar, in which only long period perturbations could be derived. Quasiperiodic fluctuations on a timescale on the order of several minutes at the peak height and the peak density of SSLs are a universal feature but could be concealed by lower temporal resolution observations (Pfrommer et al., 2009). Tsuda et al. (2011) suggested that the 7–11 min wavelike structure would be signatures of atmospheric gravity waves, while the 3 min wavelike structure may be signatures of an atmospheric gravity wave or acoustic wave. Moreover, Hansen and von Zahn (1990) analyzed sodium density data with time-resolution of 1-min and demonstrated upward and downward movements of the SSL height with the time scale of ~20 min. They also suggested that such movements are signatures of atmospheric gravity waves. However, the fine-scale ~3 min wavelike structure seems to occur locally (see Figure 3a) because the vertical and west beams do not detect such fine-scale wavelike structure in the lower layer of the SSL. In conclusion, as the lidar probes the sodium in three directions, variations will occur as the SSL is carried across the beams by the neutral wind. The changes that we see could be some combination of intrinsic temporal changes and spatial variations along the direction of advection.

As mentioned in the Section 1, horizontal advection of the SSLs was hypothesized by Clemesha et al. (1980), but they had no background wind data to confirm it. By detecting the onset time and amounts of sodium density in the SSLs via a five-direction lidar system, combined with derived background wind, Tsuda et al. (2015) verified the horizontal advection of the SSLs. However, the ending time of their SSLs was not available due to cloudy sky conditions. Since the sodium lidar observed SSLs in the vertical, and 30° off-zenith to the south and west, it is possible to assess the role of advection in the SSL variation. From Figures 3e and 3f, we observe the SSL lower layer has similar structures in the vertical and west beams, while the lifetime of the SSL is about 14.63 min in the vertical position and 12.65 min in the west position, respectively. The onset and ending time lags between the vertical and west beams are about 11 and 9.1 min, respectively. Cross-correlation analysis of the SSL upper-layer and lower-layer also indicates that both layers had a time lag of about 11 min between the vertical and west beams. The height of the SSL at 94 km corresponds to a distance of about 54.27 km between the vertical and west beams. Assuming the time lags of the SSL in the vertical and west beams are due to horizontal advection only, the bulk velocity of the SSL onset and end is estimated to be 82.2 (± 1.8) and 99.4 (± 1.8) m/s westward, respectively. These velocities are fairly consistent with the observed zonal wind velocity derived from the lidar system shown in Figure 4c (~80–90 m/s westward). This suggests that the temporal and spatial variations of the SSL are consistent with advection by the background wind.

5. Summary

A new sodium resonance fluorescence Doppler lidar system with three-directional beams has been established at Zhongshan, Antarctica. In this article, we report an SSL with spatial and temporal variations on November 14, 2019. By examining the dynamic properties of this SSL, and comparing it with a collocated E_s layer, we find the dynamic process of the SSL is closely associated with the evolution of the E_s layer.

We suggest the formation and perturbation of the SSL correlates with the convective electric field and atmospheric gravity wave activity. The onset/end of the SSL was observed by lidar at different times in the different beams, especially in the east-west direction. By using observational atmospheric wind field values obtained by the lidar system itself, we have compared wind velocities to the calculated horizontal advection effect and found the velocities are consistent. We conclude that the major source for sodium atoms in this SSL event is from the E_s layer and the dynamic properties of the SSL are modulated by the E_s layer electrodynamics and the background wind field.

Data Availability Statement

The ZHS DPS and lidar data are provided by the Polar Atmospheric and Space Physics Group, the HF radar data is from the Virginia Tech portal at <http://vt.superdarn.org/tiki-index.php?page=ASCIIData>, and Davis MF radar data is from the Australian Antarctic Data Centre (<https://data.aad.gov.au>). All these data are available from the Chinese National Arctic and Antarctic Data Center (<http://www.chinare.org.cn:8000/uap/database>).

Acknowledgments

This work is supported by the National Key Research and Development Program of China (Grant numbers 2016YFC1400300, 2021YFE0106400, and 2018YFC1407300), the National Natural Science Foundation of China (Grant numbers 41774166, 41704159, and 41831072), the International Cooperation Advance Research on Key Scientific Issues of the International Meridian Project (A131901W14), and the fund from Institute of Applied Meteorology. The author also acknowledges the use of data from the Chinese Meridian Project. SuperDARN is a collection of scientific HF radars funded by the National Science Funding Agencies of Australia, Canada, China, France, Italy, Japan, Norway, South Africa, the UK, and the USA. The operation of the Davis MF radar is supported under the Australian Antarctic Science project 4445.

References

- Batista, P. P., Clemesha, B. R., & Simonich, D. M. (1991). Horizontal structures in sporadic sodium layers at 23°S. *Geophysical Research Letters*, 18(6), 1027–1030. <https://doi.org/10.1029/91GL00549>
- Beatty, T. J., Collins, R. L., Gardner, C. S., Hostetler, C. A., Sechrist, C. F., Jr, & Tepley, C. A. (1989). Simultaneous radar and lidar observations of sporadic E and Na layers at Arecibo. *Geophysical Research Letters*, 16(9), 1019–1022. <https://doi.org/10.1029/GL016i009p01019>
- Chisham, G., Lester, M., Milan, S. E., Freeman, M. P., Bristow, W. A., Grocott, A., et al. (2007). A decade of the Super Dual Auroral Radar Network (SuperDARN): Scientific achievements, new techniques and future directions. *Surveys in Geophysics*, 28(1), 33–109. <https://doi.org/10.1007/s10712-007-9017-8>
- Chu, X., & Papen, G. (2005). Resonance fluorescence lidar for measurements of the middle and upper atmosphere. In T. Fujii & T. Fukuchi (Eds.), *Laser remote sensing* (pp. 179–432). CRC Press. <https://doi.org/10.1201/9781420030754.CH5>
- Clemesha, B. R. (1995). Sporadic neutral metal layers in the mesosphere and lower thermosphere. *Journal of Atmospheric and Terrestrial Physics*, 57(7), 725–736. [https://doi.org/10.1016/0021-9169\(94\)00049-T](https://doi.org/10.1016/0021-9169(94)00049-T)
- Clemesha, B. R., Kirchoff, V. W. J. H., Simonich, D. M., & Takahashi, H. (1978). Evidence of an extra-terrestrial source for the mesospheric sodium layer. *Geophysical Research Letters*, 5(10), 873–876. <https://doi.org/10.1029/GL005i010p00873>
- Clemesha, B. R., Kirchoff, V. W. J. H., Simonich, D. M., Takahashi, H., & Batista, P. P. (1980). Spaced lidar and nightglow observations of an atmospheric sodium enhancement. *Journal of Geophysical Research: Space Physics*, 85(A7), 3480–3484. <https://doi.org/10.1029/JA085iA07p03480>
- Collins, S. C., Plane, J. M. C., Kelley, M. C., Wright, T. G., Soldán, P., Kane, T. J., et al. (2002). A study of the role of ion–molecule chemistry in the formation of sporadic sodium layers. *Journal of Atmospheric and Solar-Terrestrial Physics*, 64(7), 845–860. [https://doi.org/10.1016/S1364-6826\(02\)00129-3](https://doi.org/10.1016/S1364-6826(02)00129-3)
- Cox, R. M., & Plane, J. M. C. (1998). An ion–molecule mechanism for the formation of neutral sporadic Na layers. *Journal of Geophysical Research: Atmospheres*, 103(D6), 6349–6359. <https://doi.org/10.1029/97JD03376>
- Croskey, C. L., Mitchell, C. N., Friedrich, M., Schmidlin, F. J., & Goldberg, R. A. (2006). Sporadic sodium and E layers observed during the summer 2002 MaCWAVE/MIDAS rocket campaign. *Annales Geophysicae*, 24, 1257–1266. <https://doi.org/10.5194/angeo-24-1257-2006>
- Dou, X. K., Xue, X. H., Chen, T.-D., Wan, W.-X., Chen, Z.-Y., Li, T., et al. (2009). A statistical study of sporadic sodium layer observed by sodium lidar at Hefei (31.8°N, 117.3°E). *Annales Geophysicae*, 27(6), 2247–2257. <https://doi.org/10.5194/angeo-27-2247-2009>
- Dou, X. K., Xue, X. H., Li, T., Chen, T. D., Chen, C., & Qiu, S. C. (2010). Possible relations between meteors, enhanced electron density layers, and sporadic sodium layers. *Journal of Geophysical Research: Space Physics*, 115(A6), A06311. <https://doi.org/10.1029/2009ja014575>
- Grebowsky, J. M., & Aikin, A. C. (2002). In E. Murat & I. P. Williams (Eds.), *Situ measurements of meteoric ions* (pp. 189–214). Cambridge University Press.
- Greenwald, R. A., Baker, K. B., Dudeney, J. R., Pinnock, M., Jones, T. B., Thomas, E. C., et al. (1995). DARN/SuperDARN: A global view of the dynamics of high-latitude convection. *Space Science Reviews*, 71(1–4), 761–796. <https://doi.org/10.1007/BF00751350>
- Hansen, G., & von Zahn, U. (1990). Sudden sodium layers in polar latitudes. *Journal of Atmospheric and Terrestrial Physics*, 52(6), 585–608. [https://doi.org/10.1016/0021-9169\(90\)90055-R](https://doi.org/10.1016/0021-9169(90)90055-R)
- Heinselman, C. J., Thayer, J. P., & Watkins, B. J. (1998). A high-latitude observation of sporadic sodium and sporadic E-layer formation. *Geophysical Research Letters*, 25(16), 3059–3062. <https://doi.org/10.1029/98GL02215>
- Kane, T. J., Gardner, C. S., Znou, Q., Mathews, J. D., & Tepley, C. A. (1993). Lidar, radar and airglow observations of a prominent sporadic Na/sporadic E layer event at Arecibo during AIDA-89. *Journal of Atmospheric and Terrestrial Physics*, 55(3), 499–511. [https://doi.org/10.1016/0021-9169\(93\)90084-C](https://doi.org/10.1016/0021-9169(93)90084-C)
- Kirkwood, S., & Collis, P. N. (1989). Gravity wave generation of simultaneous auroral sporadic-E layers and sudden neutral sodium layers. *Journal of Atmospheric and Solar-Terrestrial Physics*, 51(4), 259, 263–269. [https://doi.org/10.1016/0021-9169\(89\)90077-9](https://doi.org/10.1016/0021-9169(89)90077-9)
- Kirkwood, S., & Nilsson, H. (2000). High-latitude sporadic-E and other thin layers – The role of magnetospheric electric fields. *Space Science Reviews*, 91(3), 579–613. <https://doi.org/10.1023/A:1005241931650>
- Kirkwood, S., & Zahn, U. V. (1991). On the role of auroral electric fields in the formation of low altitude sporadic-E and sudden sodium layers. *Journal of Atmospheric and Terrestrial Physics*, 53(5), 389–407. [https://doi.org/10.1016/0021-9169\(91\)90034-5](https://doi.org/10.1016/0021-9169(91)90034-5)
- Kopp, E. (1997). On the abundance of metal ions in the lower ionosphere. *Journal of Geophysical Research: Space Physics*, 102(A5), 9667–9674. <https://doi.org/10.1029/97ja00384>
- MacDougall, J. W., & Jayachandran, P. T. (2005). Sporadic E at cusp latitudes. *Journal of Atmospheric and Solar-Terrestrial Physics*, 67(15), 1419–1426. <https://doi.org/10.1016/j.jastp.2005.07.011>

- MacDougall, J. W., Jayachandran, P. T., & Plane, J. M. C. (2000). Polar cap sporadic-E: Part 1, observations. *Journal of Atmospheric and Solar-Terrestrial Physics*, 62(13), 1155–1167. [https://doi.org/10.1016/S1364-6826\(00\)00093-6](https://doi.org/10.1016/S1364-6826(00)00093-6)
- Milan, S. E., Yeoman, T. K., Lester, M., Thomas, E. C., & Jones, T. B. (1997). Initial backscatter occurrence statistics from the CUTLASS HF radars. *Annales Geophysicae*, 15(6), 703–718. <https://doi.org/10.1007/s00585-997-0703-0>
- Murphy, D. J. (2002). Variations in the phase of the semidiurnal tide over Davis, Antarctica. *Journal of Atmospheric and Solar-Terrestrial Physics*, 64, 1069–1081. [https://doi.org/10.1016/s1364-6826\(02\)00058-5](https://doi.org/10.1016/s1364-6826(02)00058-5)
- Murphy, D. J., & Vincent, R. A. (2000). Amplitude enhancements in Antarctic MF radar echoes. *Journal of Geophysical Research: Atmospheres*, 105(D21), 26683–26693. <https://doi.org/10.1029/2000jd900510>
- Nygrén, T., Jalonon, L., Oksman, J., & Turunen, T. (1984). The role of electric field and neutral wind direction in the formation of sporadic E-layers. *Journal of Atmospheric and Terrestrial Physics*, 46(4), 373–381. [https://doi.org/10.1016/0021-9169\(84\)90122-3](https://doi.org/10.1016/0021-9169(84)90122-3)
- Nygrén, T., Voiculescu, M., & Aikio, A. T. (2008). The role of electric field and neutral wind in the generation of polar cap sporadic E. *Annales Geophysicae*, 26, 3757–3763. <https://doi.org/10.5194/angeo-26-3757-2008>
- Pfommer, T., Hickson, P., & She, C.-Y. (2009). A large-aperture sodium fluorescence lidar with very high resolution for mesopause dynamics and adaptive optics studies. *Geophysical Research Letters*, 36(15). <https://doi.org/10.1029/2009gl038802>
- Qiu, S., Soon, W., Xue, X., Li, T., Wang, W., Jia, M., et al. (2018). Sudden sodium layers: Their appearance and disappearance. *Journal of Geophysical Research: Space Physics*, 123(6), 5102–5118. <https://doi.org/10.1029/2017ja024883>
- Qiu, S., Tang, Y., & Dou, X. (2015). Temperature controlled icy dust reservoir of sodium: A possible mechanism for the formation of sporadic sodium layers. *Advances in Space Research*, 55(11), 2543–2565. <https://doi.org/10.1016/j.asr.2015.02.011>
- Qiu, S., Tang, Y., Jia, M., Xue, X., Dou, X., Li, T., & Wang, Y. (2016). A review of latitudinal characteristics of sporadic sodium layers, including new results from the Chinese Meridian Project. *Earth-Science Reviews*, 162, 83–106. <https://doi.org/10.1016/j.earscirev.2016.07.004>
- Reid, I. M., McIntosh, D. L., Murphy, D. J., & Vincent, R. A. (2018). Mesospheric radar wind comparisons at high and middle southern latitudes. *Earth Planets and Space*, 70(1). <https://doi.org/10.1186/s40623-018-0861-1>
- Reinisch, B. W., Galkin, I. A., Khmyrov, G. M., Kozlov, A. V., Bibl, K., Lisytsyan, I. A., et al. (2009). New Digisonde for research and monitoring applications. *Radio Science*, 44(1). <https://doi.org/10.1029/2008RS004115>
- Reinisch, B. W., Galkin, I. A., Khmyrov, G. M., Kozlov, A. V., Lisytsyan, I. A., Bibl, K., et al. (2008). Advancing Digisonde technology: The DPS-4D. *AIP conference proceedings* (pp. 127–143). <https://doi.org/10.1063/1.2885022>
- Ruohoniemi, J. M., & Baker, K. B. (1998). Large-scale imaging of high-latitude convection with Super Dual Auroral Radar Network HF radar observations. *Journal of Geophysical Research*, 103(A9), 20797–20811. <https://doi.org/10.1029/98ja01288>
- Simonich, D., Clemesha, B., & Batista, P. P. (2005). Sporadic sodium layers and the average vertical distribution of atmospheric sodium. *Advances in Space Research*, 35(11), 1976–1980. <https://doi.org/10.1016/j.asr.2005.06.030>
- Takahashi, T., Nozawa, S., Tsuda, T. T., Ogawa, Y., Saito, N., Hidemori, T., et al. (2015). A case study on generation mechanisms of a sporadic sodium layer above Tromsø (69.6°N) during a night of high auroral activity. *Annales Geophysicae*, 33(8), 941–953. <https://doi.org/10.5194/angeo-33-941-2015>
- Thomas, L., Gibson, A. J., & Bhattacharyya, S. K. (1977). Lidar observations of a horizontal variation in the atmospheric sodium layer. *Journal of Atmospheric and Terrestrial Physics*, 39(11–12), 1405–1409. [https://doi.org/10.1016/0021-9169\(77\)90095-2](https://doi.org/10.1016/0021-9169(77)90095-2)
- Tsuda, T. T., Nozawa, S., Kawahara, T. D., Kawabata, T., Saito, N., Wada, S., et al. (2011). Fine structure of sporadic sodium layer observed with a sodium lidar at Tromsø, Norway. *Geophysical Research Letters*, 38(18). <https://doi.org/10.1029/2011gl048685>
- Tsuda, T. T., Nozawa, S., Kawahara, T. D., Kawabata, T., Saito, N., Wada, S., et al. (2015). A sporadic sodium layer event detected with five-directional lidar and simultaneous wind, electron density, and electric field observation at Tromsø, Norway. *Geophysical Research Letters*, 42(21), 9190–9196. <https://doi.org/10.1002/2015gl066411>
- Von Zahn, U., & Hansen, T. L. (1988). Sudden neutral sodium layers: A strong link to sporadic E layers. *Journal of Atmospheric and Terrestrial Physics*, 50(2), 93–104. [https://doi.org/10.1016/0021-9169\(88\)90047-5](https://doi.org/10.1016/0021-9169(88)90047-5)
- Williams, B. P., Berkey, F. T., Sherman, J., & She, C. Y. (2007). Coincident extremely large sporadic sodium and sporadic E layers observed in the lower thermosphere over Colorado and Utah. *Annales Geophysicae*, 25(1), 3–8. <https://doi.org/10.5194/angeo-25-3-2007>
- Xue, X. H., Dou, X. K., Lei, J., Chen, J. S., Ding, Z. H., Li, T., et al. (2013). Lower thermospheric-enhanced sodium layers observed at low latitude and possible formation: Case studies. *Journal of Geophysical Research: Space Physics*, 118(5), 2409–2418. <https://doi.org/10.1002/jgra.50200>